Geophysical Journal International

*Geophys. J. Int.* (2016) **207,** 774–784
Advance Access publication 2016 August 20
GJI Marine geosciences and applied geophysics

doi: 10.1093/gji/ggw260

# Doubling the spectrum of time-domain induced polarization by harmonic de-noising, drift correction, spike removal, tapered gating and data uncertainty estimation

Per-Ivar Olsson,[1] Gianluca Fiandaca,[2] Jakob Juul Larsen,[3] Torleif Dahlin[1] and Esben Auken[2]

[1] *Teknisk Geologi, Lunds Tekniska Högskola, P.O. Box* 118, *SE-*22100 *Lund, Sweden. E-mail: per-ivar.olsson@tg.lth.se*
[2] *HydroGeophysics Group, Department of Geoscience, Aarhus University, Denmark*
[3] *Department of Engineering, Aarhus University, Finlandsgade* 22, 8200 *Aarhus N, Denmark*

Accepted 2016 July 11. Received 2016 July 8; in original form 2016 April 26

## SUMMARY

The extraction of spectral information in the inversion process of time-domain (TD) induced polarization (IP) data is changing the use of the TDIP method. Data interpretation is evolving from a qualitative description of the subsurface, able only to discriminate the presence of contrasts in chargeability parameters, towards a quantitative analysis of the investigated media, which allows for detailed soil- and rock-type characterization. Two major limitations restrict the extraction of the spectral information of TDIP data in the field: (i) the difficulty of acquiring reliable early-time measurements in the millisecond range and (ii) the self-potential background drift in the measured potentials distorting the shape of the late-time IP responses, in the second range. Recent developments in TDIP acquisition equipment have given access to full-waveform recordings of measured potentials and transmitted current, opening for a breakthrough in data processing. For measuring at early times, we developed a new method for removing the significant noise from power lines contained in the data through a model-based approach, localizing the fundamental frequency of the power-line signal in the full-waveform IP recordings. By this, we cancel both the fundamental signal and its harmonics. Furthermore, an efficient processing scheme for identifying and removing spikes in TDIP data was developed. The noise cancellation and the de-spiking allow the use of earlier and narrower gates, down to a few milliseconds after the current turn-off. In addition, tapered windows are used in the final gating of IP data, allowing the use of wider and overlapping gates for higher noise suppression with minimal distortion of the signal. For measuring at late times, we have developed an algorithm for removal of the self-potential drift. Usually constant or linear drift-removal algorithms are used, but these algorithms often fail in removing the background potentials present when the electrodes used for potential readings are previously used for current injection, also for simple contact resistance measurements. We developed a drift-removal scheme that models the polarization effect and efficiently allows for preserving the shape of the IP responses at late times. Uncertainty estimates are essential in the inversion of IP data. Therefore, in the final step of the data processing, we estimate the data standard deviation based on the data variability within the IP gates and the misfit of the background drift removal Overall, the removal of harmonic noise, spikes, self-potential drift, tapered windowing and the uncertainty estimation allows for doubling the usable range of TDIP data to almost four decades in time (corresponding to four decades in frequency), which will significantly advance the applicability of the IP method.

**Key words:** Time-series analysis; Fourier analysis; Numerical approximations and analysis; Tomography; Electrical properties.

## 1 INTRODUCTION

Recently, the interpretation and inversion of time-domain induced polarization (TDIP) data has changed as research is moving from only inverting for the integral changeability to also consider the spectral information and inverting for the full induced polarization (IP) response curves (Oldenburg 1997; Hönig & Tezkan 2007; Fiandaca *et al*. 2012, 2013; Auken *et al*. 2015). Several examples of spectral TDIP applications for different purposes have been presented (Gazoty *et al*. 2012a, 2013b; Chongo *et al*. 2015; Fiandaca *et al*. 2015; Johansson *et al*. 2015; Doetsch *et al*. 2015a,b). Furthermore, efforts have been made to achieve faster acquisitions and a better signal-to-noise ratio (SNR) by using a 100 per cent duty cycle current waveform, without current off-time (Olsson *et al*. 2015). However, drawbacks still remain for the spectral TDIP measurements, especially its limited spectral information content compared to, for example, laboratory frequency-domain spectral IP measurements (Revil *et al*. 2015). To date, only limited work has been done on increasing the spectral information content in TDIP measurement data even though recent developments in TDIP acquisition equipment have enabled access to full-waveform recordings of measured potentials and transmitted current (e.g. the Terrameter LS instrument by ABEM and the Elrec Pro instrument by Iris Instruments provide such data).

Two major limitations restrict the extraction of the spectral information of TDIP data in the field: (i) the difficulty of acquiring reliable early-time measurements in the millisecond range due to the presence of spikes and harmonic noise originating from anthropogenic sources and (ii) the self-potential background drift in the measured potentials distorting the shape of the late-time IP responses, in the second range.

Background drift in TDIP data can have multiple origins, for example, natural potential difference in the subsurface, electrochemical electrode polarization (if not using non-polarizable electrodes) and current-induced electrode polarization (if using the same electrodes for injecting current and measuring potentials). The current-induced electrode polarization drift can be orders of magnitude larger than the signal (Dahlin 2000), and thus it is crucial to compensate for this background drift in order to accurately retrieve the shape of the IP response and be able to extract the spectral IP information from TDIP measurement of the subsurface. The drift is traditionally corrected with a linear approximation (Dahlin *et al*. 2002; Peter-Borie *et al*. 2011), which for DC and integral chargeability measurements is often sufficient, but when evaluating the spectral IP information, a more accurate approximation is needed. This paper presents an improved background drift estimation method using a Cole–Cole model (Cole & Cole 1941; Pelton *et al*. 1978). This model is known accurately to describe polarization effects and it is capable of handling both linear (with long Cole–Cole time constants) and more complex non-linear drift cases such as the current-induced electrode polarization.

Spikes originating from anthropogenic sources such as electric fences for livestock management are registered by TDIP measurements. These spikes cause problems when extracting IP information, and especially spectral IP, from measured field data. This paper presents a novel and efficient processing scheme for enhancing and identifying the spikes with a series of filters applied to the raw potential signal and by implementing a flexible and data-driven threshold variable for spike identification.

Harmonic noise originates from the power supply sources oscillating at a base frequency (e.g. 50 Hz or 60 Hz) and harmonics of this base frequency. In TDIP processing today, this is handled by introducing hardware low-pass filters and/or applying rectangular gating over full period(s) of the known base frequency (e.g. 1/50 or 1/60 s). However, usage of low-pass filters or long gates cause a loss of early-time IP response information, making it difficult to resolve early-time and high-frequency spectral IP parameters. This is even more severe when the field measurements are conducted close to electric railways in countries (e.g. Austria, Germany, Norway, Sweden, Switzerland and USA) where the frequency of the power supply is even lower ($16\ ^2/_3$ or 25 Hz). This requires even longer gates to suppress the harmonic noise or a lower cut-off frequency of hardware, a low-pass filter. Deo & Cull (2015) suggested the use of a wavelet technique for de-noising TDIP data, but without retrieving IP response information at early times or high frequencies. This paper employs another method for handling the noise, which allows for use of these early times: for the first time in TDIP, a well-known method used in other geophysical disciplines for cancelling harmonic noise (Butler & Russell 1993, 2003; Saucier *et al*. 2006; Larsen *et al*. 2013) is successfully applied on full waveform data. This method models and subtracts the harmonic noise from raw full-waveform potential data. Hence, it is possible to use gate widths that are independent of the period of the harmonic noise. In reality, the earliest usable gate is then limited to when the transient electromagnetic (EM) voltage is negligible in relation to the IP voltage, considering that the EM effect is not usually modeled in the forward response. The duration of the EM effect depends on the electrode separation and the impedance of the subsurface (Zonge *et al*. 2005). Other studies have suggested methods for handling/removing the EM coupling effects (Dey & Morrison 1973; Johnson 1984; Routh & Oldenburg 2001) but this is not within of the scope of this study.

In addition to the improved background drift removal, spike removal and harmonic de-noising, this study also describes a tapered gating scheme, which is not conventional in IP applications, but has been used for decades in other geophysical methods (e.g. transient EM) for suppressing high-frequency noise (Macnae *et al*. 1984; Mccracken *et al*. 1986). Furthermore, an estimation of the data standard deviation (STD) based on the data variability within the gates and on the quality of the background drift removal is presented.

## 2 DATA ACQUISITION

Full-waveform data are very useful to facilitate digital signal processing. The required sampling rate for the full waveform depends mainly on the desired width of the shortest gate and how close it should be to the current switch off. Another consideration, which is related to the input and filter characteristics of the instrument, is that the sampling rate needs to be sufficiently high to avoid aliasing. All data presented were acquired with a 50 per cent duty cycle current waveform and 4 s on- and off-time using a modified ABEM Terrameter LS instrument for transmitting current and measuring potentials. The instrument operates at a sampling rate of 30 kHz and applies digital filtering and averaging (Abem 2011). We used a data rate of 3750 Hz, corresponding to approximately 0.267 ms per sample. Laboratory tests with frequency sweep of sinusoidal input signals showed that the in-built low-pass filter of the instrument was insufficient and would allow for severe aliasing at this sampling rate. Consequently, the instrument input filters were rebuilt by implementing fourth-order Butterworth filters with a cut-off frequency of 1.5 kHz. The instrument data rate was chosen for being able to have the first IP gate 1 ms after the turn-off of the current pulse considering that, depending on electrode separation and subsurface

resistivity (Zonge *et al*. 2005), earlier gates would likely suffer from EM effects which are not within the scope of this study.

The TDIP data were acquired along a profile (74 m, 38 acid-grade stainless steel electrodes with spacing of 2 m) laid out on a grass field in the Aarhus University campus (Denmark), with presence of multiple noise sources common in urban environments. The power-line frequency is 50 Hz (corresponding to a fundamental period of 20 ms) in all examples.

## 3 SIGNAL PROCESSING

In the field, the measured potential is composed of the sum of multiple, known and unknown, sources. To get an accurate determination of the potential response $u_{\text{response}}$, it is essential to determine and compensate for as many of these sources as possible. This is expressed as:

$$u_{\text{measured}}(n) = u_{\text{response}}(n) + u_{\text{drift}}(n) + u_{\text{spikes}}(n) + u_{\text{harmonic noise}}(n) + u_{\text{random}}(n) \quad (1)$$

where, for each sample index $n$, $u_{\text{measured}}$ is the measured potential, $u_{\text{response}}$ is the potential response from the current injection, $u_{\text{drift}}$ is the background drift potential, $u_{\text{harmonic noise}}$ is the harmonic noise from AC power supplies and $u_{\text{random}}$ is the potential from other random and unknown sources. The component $u_{\text{random}}$ represents random background noise and is most efficiently handled by gating and stacking. The known noise sources in eq. (1) ($u_{\text{drift}}$, $u_{\text{spikes}}$ and $u_{\text{harmonic noise}}$) can be handled separately and removed in a sequential manner with the processing scheme described in this study. A method for estimating the uncertainty of the processed data is presented also. For continuity, the different parts of the signal processing scheme in this section are presented using one full-waveform potential (and current) recording acquired as described in the previous section. However, due to absence of anthropogenic spikes in this recording, another full waveform acquired in a rural area in western Denmark is used for the de-spiking example in Fig. 3.

### 3.1 Linear drift removal, stacking and rectangular gating

The recording of full-waveform data allows for stacking and gating of the data originating from different current pulses with any distribution of the IP gates after acquisition, the only limitation being the acquisition sampling rate. In this study, extraction of the potential response down to 1 ms after the current turn-off is desired. This is achieved by using a delay of 1 ms after the current turn-off and applying a log-increasing gating scheme, which compensates for changes of SNR throughout the IP response (Gazoty *et al*. 2013). When the gates are wide enough (i.e. equal to or wider than 20 ms) the gate widths are rounded off to multiples of the period of the harmonic noise (Table 1, seven gates per decade).

The stacking and gating procedure classically used for retrieving the IP responses from the full-waveform data is carried out according to:

$$u_{\text{IP,stacked}}(k) = \frac{1}{N_{\text{pulses}}} \sum_{j=1}^{N_{\text{pulses}}} (-1)^{j+1} u_{\text{processed}}(k + S_{\text{IP}}(j) - 1) \quad (2)$$

$$u_{\text{IP,gated}}(m) = \frac{1}{N_{\text{samples}}(m)} \sum_{i=1}^{N_{\text{samples}}(m)} u_{\text{IP,stacked}}\left(i + S_{\text{gate}}(m) - 1\right) \quad (3)$$

where $u_{\text{IP,stacked}}$ and $u_{\text{IP,gated}}$ are the stacked and gated potential respectively; $k$ is the sample index of the stacked IP response; $m$ is the gate index; $N_{\text{pulses}}$ and $N_{\text{samples}(m)}$ are the number of pulses and gate samples, respectively; $u_{\text{processed}}$ represents the measured potential after some processing (typically after drift correction); $S_{\text{IP}}(j)$ is the first sample index of the IP signal for pulse number $j$ and $S_{\text{gate}}(m)$ is the first sample index in gate $m$. Eq. (2) is thus the stacking procedure that makes use of the negative and positive signs of the pulses and eq. (3) defines rectangular gates on the signal.

In analogy to eq. (3), the DC potential, $u_{\text{DC,gated}}$ is averaged over all pulses and used for normalizing the IP response according to eq. (4):

$$u_{\text{IP,normalized}}(m) = \frac{u_{\text{IP,gated}}(m)}{u_{\text{DC,gated}}}. \quad (4)$$

Fig. 1 shows both the full-waveform acquisition (top) and the corresponding decay (bottom) for an exemplary recording of the data measured along the test profile at the Aarhus Campus. The full-waveform potential clearly shows the presence of $u_{\text{drift}}$, $u_{\text{spikes}}$, $u_{\text{harmonic noise}}$ and $u_{\text{random}}$ superposed to $u_{\text{response}}$. In fact, the signal presents an overall increasing trend (the drift), big positive and negative variations at the current turn-on and turn-off, spikes (both in the potential and current recording) and fast oscillations that mask completely the IP response (harmonic and random noise).

Traditionally, the drift is removed using synchronous detection designed so it either removes static shifts, or if a bit more advanced, linear trends (Dahlin *et al*. 2002; Peter-Borie *et al*. 2011), while the other noise sources are handled by the stacking/gating procedure.

In Fig. 1 (bottom), two responses are shown: the resulting IP response (green) after gating and stacking the full-waveform potential according to eqs (3) and (4) and Table 1, as well as the IP response retrieved using the default gating in the instrument with gates multiple of 20 ms (magenta). In both cases, the signal is corrected for linear drift $u_{\text{drift}}(n) = a * n + b$. The re-gated IP response shows similar magnitude as the instrument supplied after approximately 60 ms, when the gates for both responses are multiples of 20 ms. Contrastingly, it exhibits an erratic behaviour until 60 ms since the gates are not 20 ms multiples and the harmonic noise is not suppressed. Clearly, the harmonic noise needs to be assessed in order to be able to use gates, which are shorter than 20 ms. Also note that the tail of both IP responses is increasing at the end. This paper will show that this is a result of poor performance of the background drift removal when applying a linear drift model.

### 3.2 Cole–Cole model-based drift removal

The background drift, $u_{\text{drift}}$, is made up of two components, self-potentials in the Earth (Dahlin *et al*. 2002) and electrode polarization (Dahlin 2000). While the linear drift removal works reasonably well for compensation of self-potentials, it is not optimal for compensation of potentials due to electrode polarization. The electrode polarization is typically attributed to charge buildup on the interface between the conducting metal of the electrode and the surrounding ground of less conductance. These effects can be orders of magnitude larger than the IP signal, when an electrode is used for transmitting current, and are clearly not linear (Dahlin 2000). Electrode polarization is hard to avoid due to difficulties of designing meaningful measurement sequences that do not use electrodes for potential measurements shortly after they have been

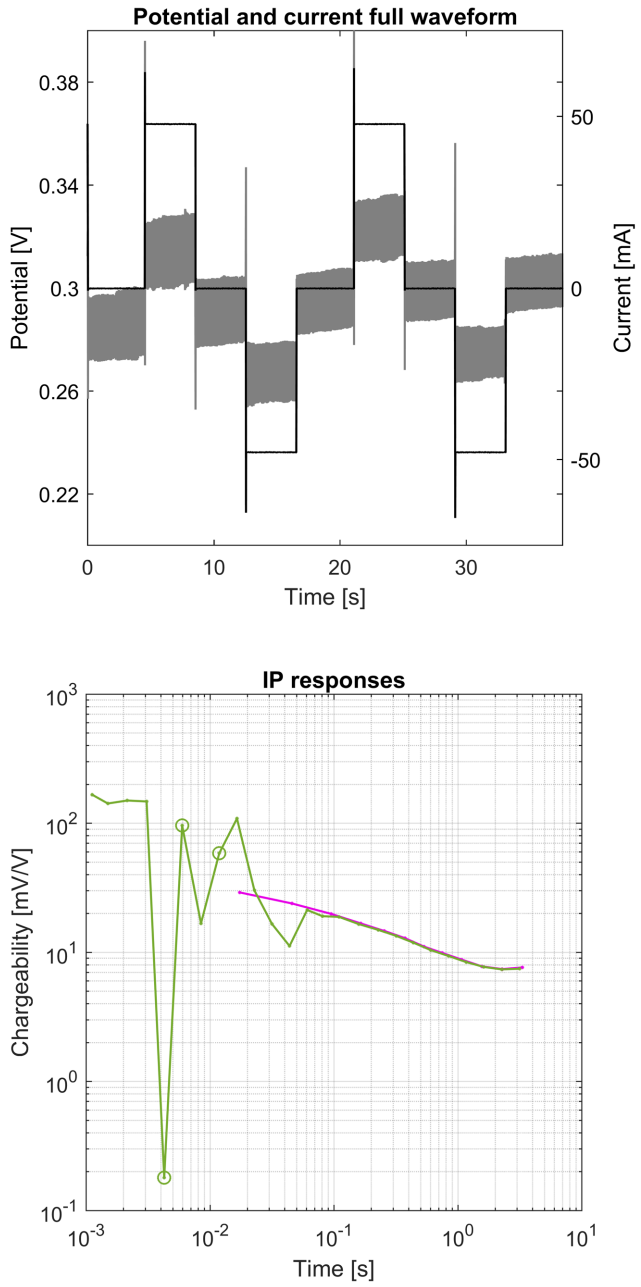


**Figure 1.** Top: 50 per cent duty cycle raw full-waveform potential data (grey) and transmitted current (black). Bottom: IP response binned with gates that are multiples of 20 ms and delay of 10 ms (magenta, instrument output) and re-gated IP response according to Table 1 and linear drift removal (green data points indicated by o-marker are negative). Note that the green response exhibits erratic behaviour in the beginning, while the gates are not multiples of the time period of the harmonic noise. Also note that the tail of both IP responses shows an increase in chargeability.

used for current injections. Electrode contact tests performed before initiating the TDIP measurements are also an important source for electrode polarization. Consequently, for compensating the background drift it is important to use a drift model that accounts for the polarization phenomenon at the electrodes. In this study, we use a drift model (eq. 5) based on the Cole–Cole model (Cole & Cole 1941; Pelton *et al*. 1978), because the Cole–Cole model well describes depolarization phenomenon and several tests on field data from different surveys proved the efficiency of the $u_{\text{drift}}$ model of eq. (5) in removing the drift:

$$u_{\text{drift}}(n) = m_0 \sum_{j=0}^{\infty} (-1)^j \left(\frac{n}{\tau f_s}\right)^{jc} \Gamma(1+jc)^{-1} + d \qquad (5)$$

where $n$ represents the sample index; $d$ is an offset constant; $f_s$ is the sampling frequency; $m_0$ is the drift amplitude; $\tau$ is the Cole–Cole relaxation time; $c$ is the Cole–Cole frequency exponent and $\Gamma$ is Euler's Gamma function $\Gamma(x) = \int_0^\infty y^{x-1}e^{-y}dy$. Thus, eq. (5) corresponds to the Cole–Cole model as described by Pelton *et al*. (1978) with an added offset constant $d$.

The fitting of the drift model parameters is conducted on a gated subset of the full-waveform signal ($u_{\text{subset}}$). The width of the gating window is set to a full period (e.g. 20 ms for 50 Hz) of the fundamental frequency of the power-line harmonic so that the harmonic oscillations are suppressed.

$$u_{\text{subset}}(i) = \frac{1}{N_{f0\ \text{samples}}} \sum_{j=1}^{N_{f0\ \text{samples}}} u_{\text{measured}}(S_{\text{subset}}(i) + j - 1) \qquad (6)$$

where $u_{\text{subset}}(i)$ is the $i$th datum of the drift subset, $N_{f0\ \text{samples}}$ is the number of samples corresponding to the time period of the fundamental frequency and $S_{\text{subset}}(i)$ represents the first sample index used for gating $u_{\text{measured}}$ and retrieving $u_{\text{subset}}(i)$. For increased computing speed when fitting the $u_{\text{drift}}$ model parameters, and since the drift is smoothly varying, the $S_{\text{subset}}$ variable is selected so that $u_{\text{subset}}$ only consists of 4–10 points per second.

Since the IP responses themselves create an offset from the drift baseline, the drift model fit is done on a subset of the gated signal ($u_{\text{subset}}$, eq. 6). This subset is taken from the end of the off-time period for the 50 per cent duty cycle (orange x-marker, Fig. 2) where the effect of the IP responses on the drift baseline is smaller. For the 100 per cent duty-cycle current waveform, the subset is taken at the end of the on-time period. Even if there is residual IP signal ($u_{\text{response}}$) in $u_{\text{measured}}$ where the $u_{\text{subset}}$ is taken, the alternating positive–negative character of the current pulses will cause also the IP offset to alternate around the drift baseline. Owing to this, the drift estimate method is not significantly sensitive to residual IP signal in the $u_{\text{subset}}$ data, since the fit of $u_{\text{drift}}$ goes in between the positive–negative residual IP signals.

For the drift subset data used in this paper, $u_{\text{subset}}$ (orange x-marker, Fig. 2) corresponds to 4 points per second for the last 40 per cent of each off-time period, except for the first off-time period (before the first pulse) where it corresponds to the last 70 per cent.

Fig. 2 shows examples of estimated drift models, as well as the resulting IP responses after gating and stacking. In the drift model and full-waveform potential plot (Fig. 2, top), there is a significant difference between the linear fit model (green) and the data actually used for estimating the drift (orange x-markers). Clearly, the linear model is not sufficient for describing the drift accurately and it gives increasing chargeability values for the late gates (green line; Fig. 2, bottom). During the off-time, the potential should monotonically tend to 0 at late times independent of subsurface chargeability distribution in time and space. Contrastingly to the linear drift model, the Cole–Cole model (blue line; Fig. 2, bottom) shows a good fit of the drift and the resulting IP response does not show a chargeability increase at late times. Consequently, it is clear that a linear drift model gives incorrect IP responses at late times and that a more advanced drift model such as the Cole–Cole model is necessary. It is also clear that especially the gates at late times, with low 'signal-to-drift' ratios, are affected by the drift model accuracy.

**Table 1.** Duration of delay time and IP gates for the processed field data corresponding to seven gates per decade. Note that gates from 13 and higher have widths which are multiples of 20 ms.

| **Gate number** | **Delay** | **1** | **2** | **3** | **4** | **5** | **6** | **7** | **8** | **9** | **10** | **11** | **12** |
|---|---|---|---|---|---|---|---|---|---|---|---|---|---|
| **Width (ms)** | 1 | 0.26 | 0.53 | 0.80 | 1.06 | 1.33 | 2.13 | 2.93 | 4 | 5.33 | 7.46 | 10.4 | 14.4 |
| **Gate number** | **13** | **14** | **15** | **16** | **17** | **18** | **19** | **20** | **21** | **22** | **23** | **24** | **25** |
| **Width (ms)** | 20 | 20 | 40 | 60 | 60 | 120 | 120 | 180 | 300 | 360 | 540 | 780 | 1020 |

### 3.3 Removal of spikes

De-spiking of the signal is done for two reasons. The first reason is that potential spikes can result in a shifted average value of a given gate. Since the spikes normally last for a fraction of a millisecond, and have an average close to zero (bipolar spikes), this problem is not so pronounced for long gates where all samples of an individual spike fall within the gate. However, for short gates consisting of a few samples, only parts of the spike might fall within the gate and thus the spike has a large effect on the average value. The second reason for eliminating the spikes is related to the subsequent modelling of the harmonic noise, which is known to be sensitive to spikes in the data (Dalgaard *et al*. 2012).

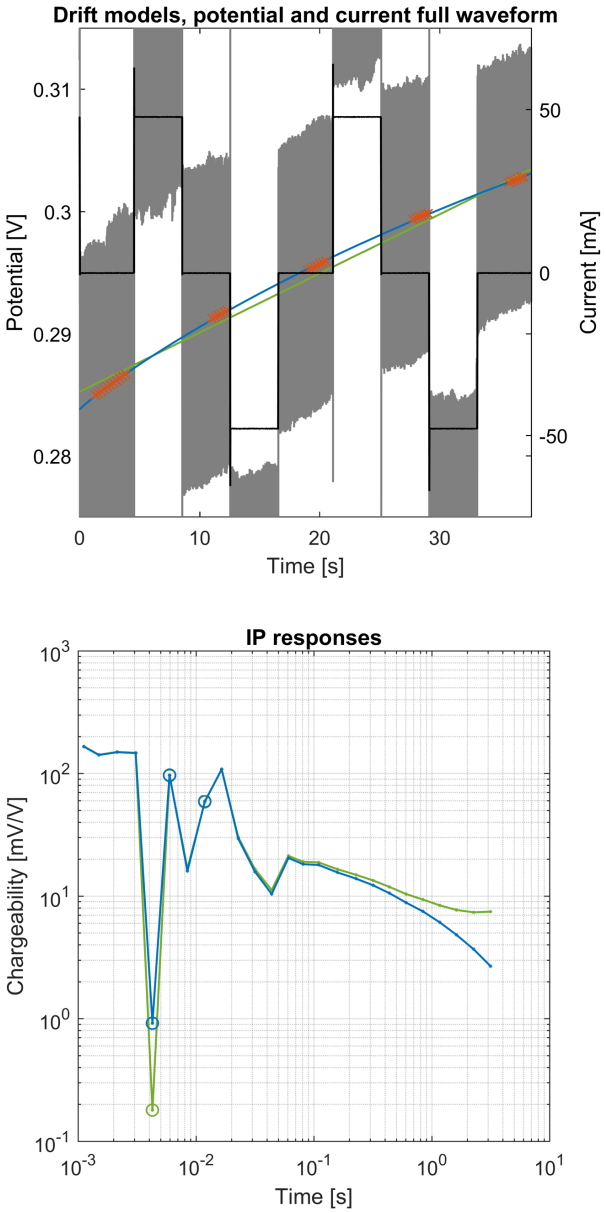


**Figure 2.** Top: 50 per cent duty cycle raw full-waveform potential data (grey) and transmitted current (black), subset of the signal used for finding the drift model (orange x-marker) and different types of background drift models (green: linear model and blue: Cole–Cole model). Bottom: resulting gated IP response curves (green: linear model and blue: Cole–Cole model. Negative values are marked with o-markers). Note that the resulting shapes of the IP responses are highly dependent on the used drift model at the later gates.

Before the de-spiking can be carried out, an accurate and robust method for identifying the spikes is needed. Our method uses several steps to enhance the spikes in the signal and defines a data-driven, automatic threshold to determine if a sample index ($n$) is to be considered as spike or not:

(1) A simple first-order high-pass filter (eq. 6) is applied on the full-waveform potential ($u_{\text{measured}}(n)$, shown in the top panel in Fig. 3) for removing signal offset and enhancing spike visibility:

$$u_2(n) = u_{\text{measured}}(n) - u_{\text{measured}}(n-1). \quad (7)$$

(2) The spikes are further enhanced by applying a non-linear energy operator, which is known to give a good estimate of signal energy content (Kaiser 1990; Mukhopadhyay & Ray 1998) on the output from step 1 ($u_2$, mid panel in Fig. 3) and by taking the absolute value (eq. 7):

$$u_3(n) = abs\left(u_2(n)^2 - u_2(n-1)\,u_2(n+1)\right). \quad (8)$$

(3) The signal $u_3$ (black line, lower panel in Fig. 3) is downsampled by taking the maximum value within 20 ms segments.

(4) A Hampel filter (Davies & Gather 1993; Pearson 2002) is applied on the output from step 3. The Hampel filter computes the median of the sample and its neighbour samples (four on each side in our examples) and estimates the STD by a mean absolute deviation. If the sample value differs more than 3 STDs from median, the sample value is replaced with the median.

(5) The output from step 4 is interpolated with linear interpolation for each sample index in $u_3$.

With these steps, an automatic data-driven threshold for spikes is defined, as shown in Fig. 3 (lower panel, orange curve). All the samples above the threshold are flagged as spikes (Fig. 3, orange o-marker) and are neglected when performing the harmonic de-noising procedure, thereafter the de-spiking is done based on the harmonic de-noised signal.

The de-spiking is done as a last step of the overall signal processing, after the cancelling of harmonic noise, by replacing spike-flagged sample values with the median of its eight neighbouring samples (four on each side) in the processed potential ($u_{\text{processed}} = u_{\text{measured}} - u_{\text{drift}} - u_{\text{harmonic noise}}$). The routine identifies spikes during both the on- and off-time of the current injections (Fig. 3, orange o-marker) as well as spikes originating from when the current is switched (Fig. 3). The current switch spikes, often originating from EM effects, are considered as spikes for the succeeding harmonic de-noising, but they are not included when replacing the values of the spike samples as described in previous section.

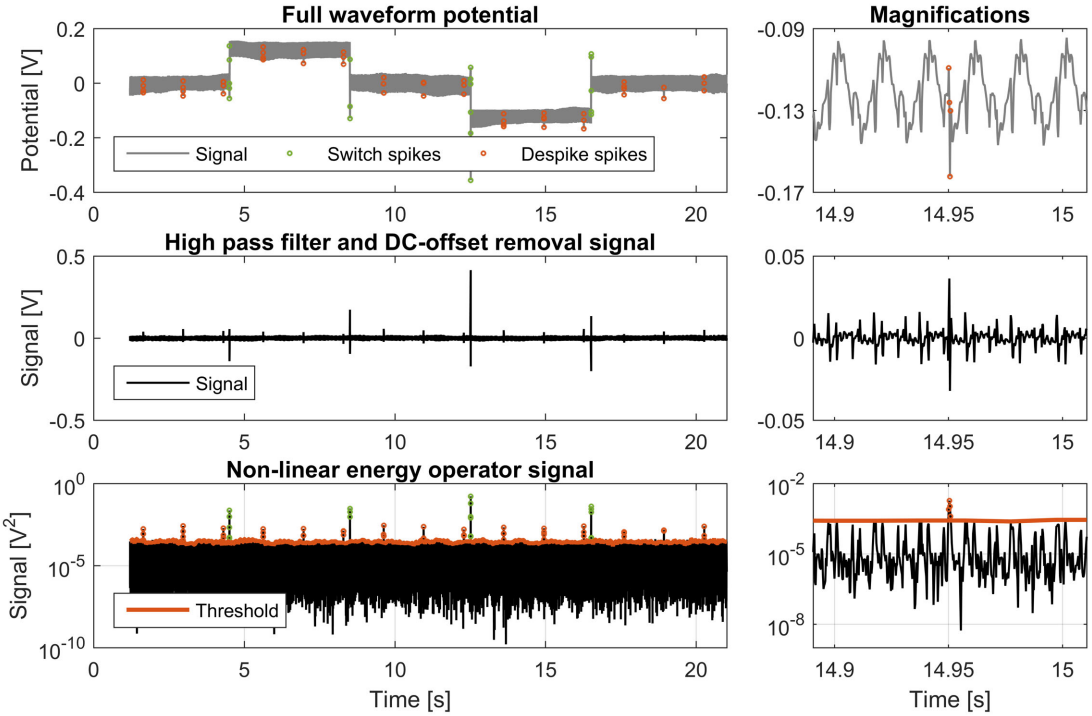


**Figure 3.** Top: identified spike samples of a full-waveform potential signal. Mid: output from applied high-pass and offset removal filter. Bottom: output from non-linear energy operator filter, spike samples and threshold value (bottom). Samples marked as 'switch spikes' corresponds to spikes identified at discontinuities from current switches while 'despike spikes' corresponds to other identified spikes in the signal. Magnifications of the 11th identified de-spike–spike (from 14.891 to 15.011 s) are shown on the right.

However, the current switch spike information is used in this paper for full rejection of IP gates that contains samples flagged as switch spikes.

### 3.4 Model-based cancelling of harmonic noise

We have adapted the approach for harmonic noise removal as presented for magnetic resonance soundings by Larsen *et al.* (2013) and seismoelectrics by Butler & Russell (1993). Typical harmonic noise originates from the power distribution grid or from AC train power distribution. The method describes the harmonic noise in terms of a sum of harmonic signals having frequencies given by a common fundamental frequency ($f_0$) multiplied with an integer ($m$) but with independent amplitudes ($\alpha_\mathrm{m}$ and $\beta_\mathrm{m}$) for each harmonic $m$:

$$u_{\text{harmonic noise}}(n) = \sum_m \left( \alpha_m \cos\left(2\pi m \frac{f_0}{f_s} n\right) + \beta_m \sin\left(2\pi m \frac{f_0}{f_s} n\right)\right). \quad (9)$$

By accurately determining the harmonic parameters $f_0$, $\alpha_\mathrm{m}$ and $\beta_\mathrm{m}$, it is possible to describe precisely the harmonic noise component of the measured potential and to subtract it from $u_{\text{measured}}$. However, the parameters $f_0$, $\alpha_\mathrm{m}$ and $\beta_\mathrm{m}$ are not constant for the timescale (seconds to minutes depending on acquisition settings) of a TDIP measurement and the frequency can generally vary up to $\pm 0.1$ Hz in such a time frame in Nordic countries (Li *et al.* 2011). It has been shown that the fundamental frequency needs to be estimated with an accuracy of a few millihertz (Larsen *et al.* 2013). This accuracy is obtained by dividing the signal into shorter segments assuming the variation of the fundamental frequency in each segment is negligible. Butler & Russell (1993) show that the error of the harmonic parameters decreases with increasing segment length and that the best parameters are achieved when the segment length is a multiple of the period of the fundamental frequency (e.g. 20 ms multiples for $f_0 = 50$ Hz). Experience from processing several different TDIP data sets has shown that a segment length including overlap in the range of 200–300 ms is suitable for achieving good estimates and harmonic parameters, while a segment length of 220 ms with an overlap of 20 ms was used in this paper.

After segmenting the full-waveform potential, the noise model parameters are found by minimizing the residual $E_{\text{residual}}$ after subtracting a temporary harmonic noise model from the drift-corrected full-waveform potential segment (ignoring identified spike samples):

$$E_{\text{residual}} = \sum_n \left(u_{\text{measured}}(n) - u_{\text{drift}}(n) - u_{\text{harmonic noise}}(n)\right)^2. \quad (10)$$

The minimum residual for each segment is determined with an iterative approach using golden section search and parabolic interpolation (Forsythe *et al.* 1977) for minimizing $E_{\text{residual}}$ by changing the fundamental frequency within a given interval around the expected frequency (e.g. $50 \pm 0.2$ Hz). For processing efficiency, a subset of the harmonics is used for the noise model when determining fundamental frequency. This subset is chosen by taking the $m_{\text{high}}$ harmonics with the highest estimated power spectral density energy (green o-marker in Fig. 4 where $m_{\text{high}} = 10$) compared to the baseline energy (general energy trend if ignoring the peaks). Finally, after identifying the fundamental frequency for a segment, the $\alpha_\mathrm{m}$ and $\beta_\mathrm{m}$ parameters are recalculated for all harmonics up to $f_\mathrm{s}/2$, that is, half of the sampling frequency (Fig. 5, showing $\alpha_1$ and $\beta_1$).

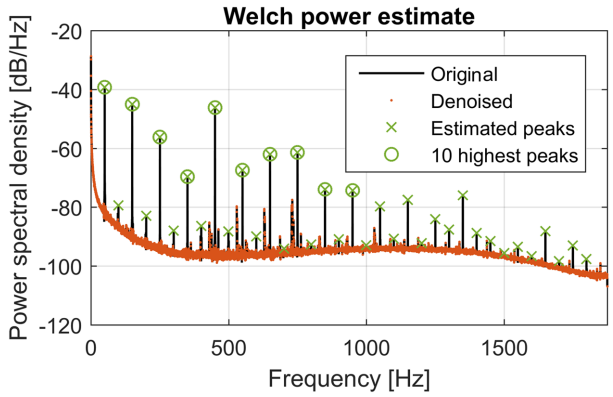


**Figure 4.** Welch power estimate of a full recording of potential for one quadruple: original signal (black), residual signal after noise cancellation (orange). The green markers show identified energy peaks (cross marker) and harmonics used for finding the fundamental frequency (circle marker). There is a clear reduction of the energy at 50 Hz and its harmonics after the processing and the energy level is reduced to the baseline. The remaining energy peaks represent frequencies that are not harmonics of the 50 Hz.

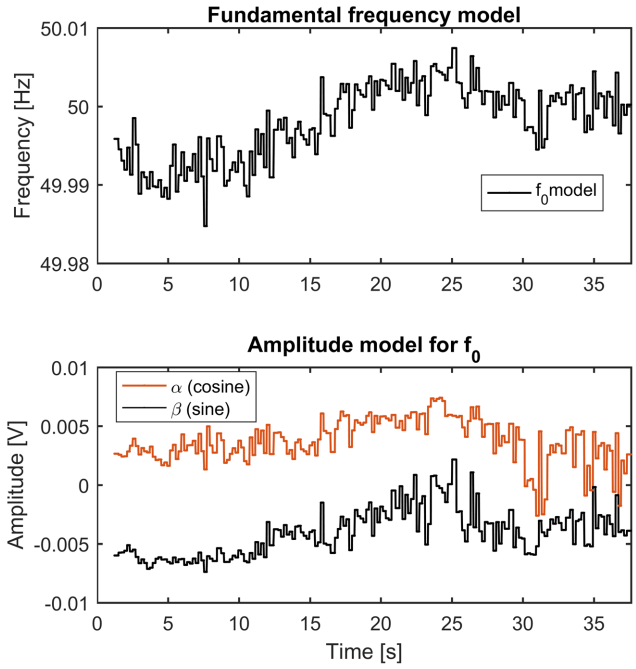


**Figure 5.** Top: example of parameters for a harmonic noise model, showing the model for the fundamental frequency. Bottom: amplitude models for $\alpha$ and $\beta$ for the fundamental frequency corresponding to eq. (8) with $m = 1$.

Fig. 4 shows the Welch power spectral density estimate (Welch 1967), which gives an estimate of the signal power for different frequencies, for a full-waveform potential recording before and after applying the harmonic de-noising. The original signal (black line) exhibits distinct peaks of energy at 50 Hz and integer multiples of this frequency corresponding to the harmonics. In the corresponding energy estimate after the harmonic de-noising (orange line), the energy peaks have been reduced to the baseline energy as a result of modelling and subtracting the harmonic noise. The remaining energy peaks after harmonic de-noising (e.g. at approximately 430, 630 and 780 Hz) represent frequencies that are not harmonics of the 50 Hz.

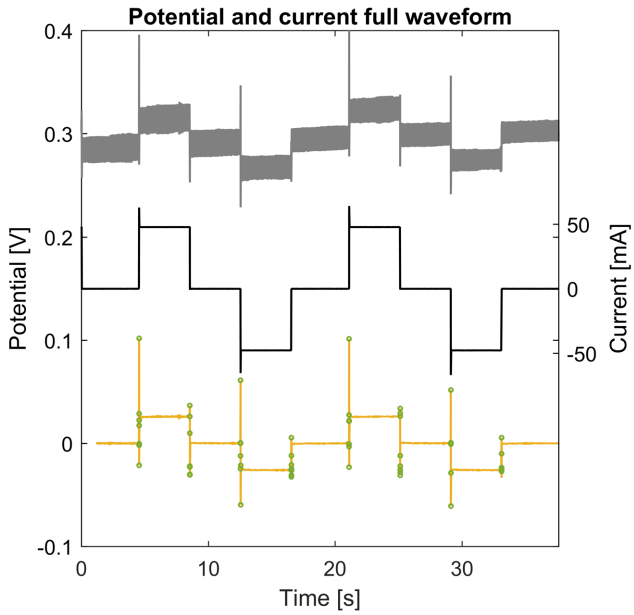


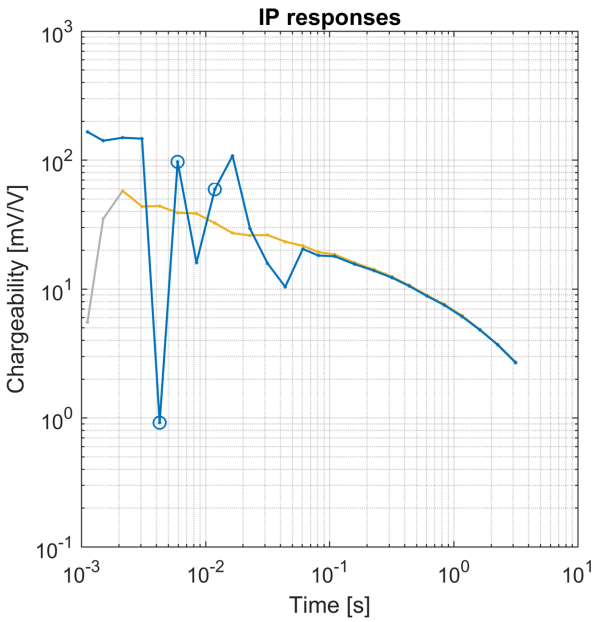


**Figure 6.** Top: full-waveform current (black) and potential before (grey) and after (yellow) drift removal and cancelling of harmonic noise. Switch spike samples are indicated by green o-marker. Bottom: resulting IP responses with harmonic denoising (yellow line, gates associated with indicated switch spikes are shown in grey) and without (blue line).

Fig. 6 shows the data from Fig. 2, but now corrected for Cole–Cole drift, spikes and harmonic noise according to eqs (3) and (4) ($u_{\text{processed}} = u_{\text{measured}} - u_{\text{drift}} - u_{\text{spikes}} - u_{\text{harmonic noise}}$). The resulting IP response with harmonic de-noising (Fig. 6, bottom, yellow line) shows a clear improvement compared to the IP response without the harmonic de-noising (blue line). The erratic behaviours for early gates are absent and the IP response shows a decaying shape, as it is expected for a survey on a generally homogeneous media (see Section 4). These improvements extend the first usable spectral IP information to around 2 ms after the current pulse. The first two gates (grey line) show an unexpected behaviour with increasing values also after applying the harmonic de-noising. This behaviour

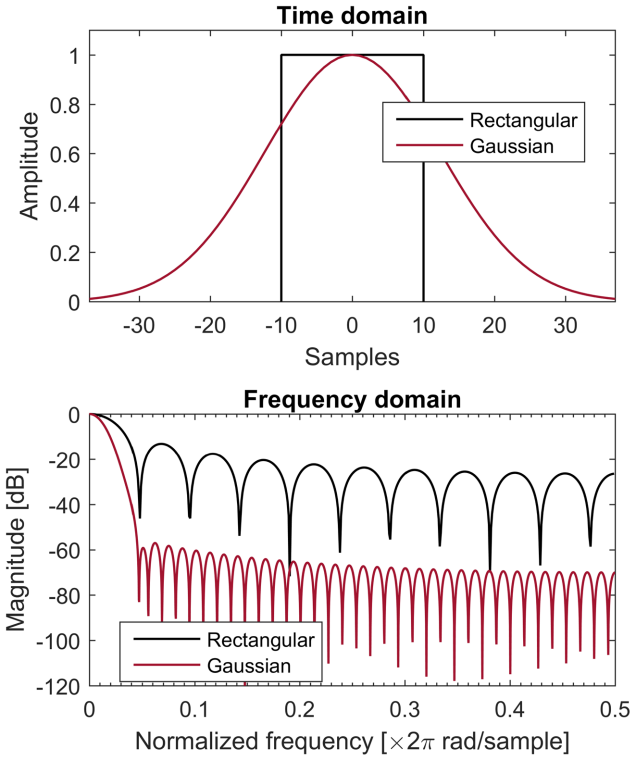


**Figure 7.** Time-domain (top) and frequency-domain (bottom) representations of rectangular (21 samples) and Gaussian ($N_{\text{window}} = 75$ samples and $\alpha = 3$, i.e. 3 standard deviations contained in the window) windows. Note that in frequency domain, the side lobes have Fourier transform magnitudes approximately 40 dB lower for the Gaussian window.

is due to a presence of spikes in the measured voltage (yellow line and green o-marker, Fig. 6 top) in these gates and thus these gates are rejected by the processing.

### 3.5 Tapered gate design and error estimation

Today, the standard procedure for gating IP is to average the data within the pre-defined IP gates, corresponding to a discrete convolution with a rectangular window. In other geophysical methods (e.g. transient EMs) different kinds of tapered windows have been used for decades for gating data (Macnae *et al*. 1984; Mccracken *et al*. 1986). One reason for using tapered window functions is that the suppression of high-frequency noise is superior in comparison with the rectangular one. Furthermore, the tapered windows allow the use of wider and overlapping gates, which have higher noise suppression, with minimal distortion of the signal. An example of this effect is seen in Fig. 7 where the filter characteristic of a rectangular window (black line) is compared with a wider (3.5 times) Gaussian window (red line) in time and frequency domains. The Gaussian window coefficients $w_m$ for gate $m$ are given by (Harris 1978):

$$w_m(i) = e^{-\frac{1}{2}\left(\alpha \frac{i}{(N_{\text{window}}(m)-1)/2}\right)^2}; |i| \leq (N_{\text{window}}(m) - 1)/2 \qquad (11)$$

where $i$ is window sample index, $N_{\text{window}}(m)$ is total number of window samples for gate $m$ and $\alpha$ is the number of STDs contained in the window ($\alpha = 3$ in our example, i.e. 3 STDs contained in the window).

In the frequency domain, the main lobe of both windows cuts at approximately the same normalized frequency (because of the increased width of the Gaussian window, otherwise the Gaussian window would cut at higher frequencies), but the side lobes of the Gaussian window are around 40 dB smaller. Thus, the Gaussian window is superior in reducing the high-frequency noise contribution ($u_{\text{random}}$) compared to the rectangular window. Consequently, we have chosen to implement the tapered gates using overlapping Gaussian-shaped windows which are 3.5 times wider than the gate widths of Table 1 ($N_{\text{window}}(m) = 3.5 * N_{\text{samples}}(m)$), but with the same centre times. However, in this study, the tapered gating is not used directly for signal estimation: a more sophisticated approach is developed for better estimating both the signal itself and its uncertainty from the data variability within the gates.

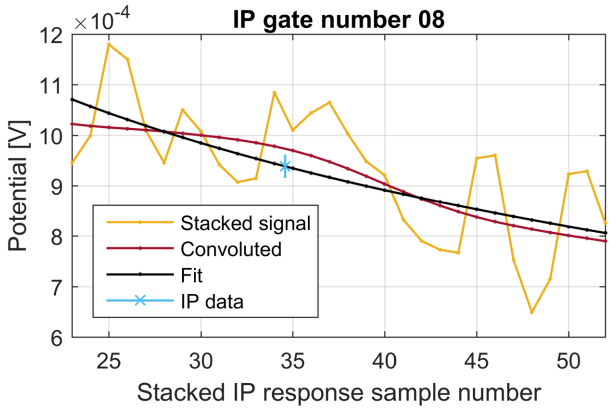


**Figure 8.** The different steps involved in tapered gating and error estimation for gate number 8 of the processing example. Final IP gate datum with corresponding STD estimate of the gating uncertainty is shown in light blue.

Uncertainty estimation of the data for individual IP gates cannot be retrieved by directly comparing the individual IP stacks since, for the finite number of pulses used in field surveys, each individual pulse response is different due to superposition from previous pulses (Fiandaca *et al*. 2012), hence other approaches are needed. The variability of the signal within the gates is a valuable option, and it is also desirable that the uncertainty estimate makes use of the actual window function used when gating the data. With sufficient gates per decade used for gating the data, the signal variability is almost linear within the gates and for IP signals the linearity is more evident in lin–log space (corresponding to exponential in lin–lin space), except for the presence of noise. Thus, it is possible to convolve the signal within the gates with the Gaussian windows (eq. 11) for suppressing the noise and to use the misfit of an exponential fit of the convoluted data in for estimating the gate uncertainty.

Fig. 8 shows the different steps for estimating the signal and its gating uncertainty using the eighth gate of the response of Fig. 6 as an example:

- First, the $u_{\text{IP,stacked}}$ signal is computed from the full-waveform data processed with Cole–Cole drift removal, de-spiking and harmonic de-noising according to eq. (2) (yellow line).
- After stacking, the convolution for gate number $m$, $u_{\text{IP,conv}(m)}$ of the stacked potential, $u_{\text{IP,stacked}}$ is determined according to eq. (11) (red line):

$$u_{\text{IP,conv}(m)}(j) = \frac{1}{\sum w_m} \sum_{i=-\frac{N_{\text{window}}(m)-1}{2}}^{\frac{N_{\text{window}}(m)-1}{2}} u_{\text{IP,stacked}}\left(j + S_{\text{gate}}(m) - 1 - i\right) w_m(i) \qquad (12)$$

where $j$ denotes sample index within the gate $m$.

- An exponential fit of convoluted signal is done in lin—lin space (denoted $u_{\mathrm{IP,fit}(m)}$, black line).
- The IP value for the gate is retrieved by evaluating the exponential fit at the log-centre time of the gate (light blue x-marker).
- Last, the gating STD on the value, $\mathrm{STD}_{\mathrm{gating}}(m)$ (light blue error bar) is computed in terms of misfit between convoluted data and exponential fit for all the gate samples ($N_{\mathrm{samples}}(m)$), as follows in eq. (12):

$$\mathrm{STD}_{\mathrm{gating}}(m) = \sqrt{\frac{1}{N_{\mathrm{samples}}(m)} \sum_{i=1}^{N_{\mathrm{samples}}(m)} \left(u_{\mathrm{IP,conv}(m)}(i) - u_{\mathrm{IP,fit}(m)}(i)\right)^2}. \quad (13)$$

This estimate gives a measure of the noise content within the gate after the convolution. In fact, whenever the noise level is low and enough gates per decade are used (i.e. normally 7–10), the misfit is negligible. Contrastingly, if random or residual harmonic noise or both are present, the misfit between the convoluted signal and the exponential fit represents a measure of the gating uncertainty. By using the convoluted gate signal for estimating the uncertainty, the measure takes into account the convolution used in the processing.

The STD computed from the data gating is not the only uncertainty estimation linked to the processing scheme presented in this study. As shown in Fig. 2, also the background drift removal can have a large impact on the resulting IP responses and the fit of the drift model gives a useful measure of the remaining drift uncertainty. Similarly to the estimation of gating uncertainty, the drift uncertainty ($\mathrm{STD}_{\mathrm{drift}}$) is estimated from the sum of misfit between drift subset data ($u_{\mathrm{subset}}$, orange x-marker in Fig. 2) and Cole–Cole drift fit ($u_{\mathrm{drift}}$, blue line in Fig. 2) for all drift subset data samples ($N_{\mathrm{subset}}$) according to eq. (13)

$$\mathrm{STD}_{\mathrm{drift}} = \frac{1}{N_{\mathrm{subset}}} \sqrt{\sum_{i=1}^{N_{\mathrm{subset}}} \left(u_{\mathrm{subset}}(i) - u_{\mathrm{drift}}(n_{\mathrm{drift}}(i))\right)^2} \quad (14)$$

where $n_{\mathrm{drift}}(i)$ gives the global sample index $n$ for drift subset data point $i$.

The total uncertainty ($\mathrm{STD}_{\mathrm{total}}$) for any IP gate is computed by summing up the gating, drift and a uniform STD according to eq. (14)

$$\mathrm{STD}_{\mathrm{total}}(m) = \sqrt{\mathrm{STD}_{\mathrm{gating}}(m)^2 + \mathrm{STD}_{\mathrm{drift}}^2 + \mathrm{STD}_{\mathrm{uniform}}^2} \quad (15)$$

Finally, Fig. 9 shows the processed IP response in terms of values and relative total STDs (with 5 per cent of uniform STD) in comparison with the IP response as supplied by processing of the instrument. The STD error bars increase at early times since the shorter gates give higher $\mathrm{STD}_{\mathrm{gating}}$, while at late times the drift uncertainty increases and $\mathrm{STD}_{\mathrm{drift}}$ contributes more to the total gate $\mathrm{STD}_{\mathrm{total}}$. Note that error bars with the total error captures the fluctuations in chargeability. The two first gates are artefacts created by the potential spikes at the polarity switches of the pulses and rejected by the processing for containing switch spikes (Figs 2 and 6). Nevertheless, the first reliable gate (gate number 3) corresponds to approximately 2 ms after the current pulse, compared to 20 ms for the instrument output.

The presented processing scheme includes assumptions that are not always fulfilled in field applications. In particular, the parameters of the harmonic noise model are assumed to be constant within each segment in which the signal is subdivided and rapidly varying parameters are not entirely compensated. However, the proposed uncertainty estimation takes into account the performance of the processing scheme and ineffective harmonic de-noising or drift removal will be reflected in the data error bars.

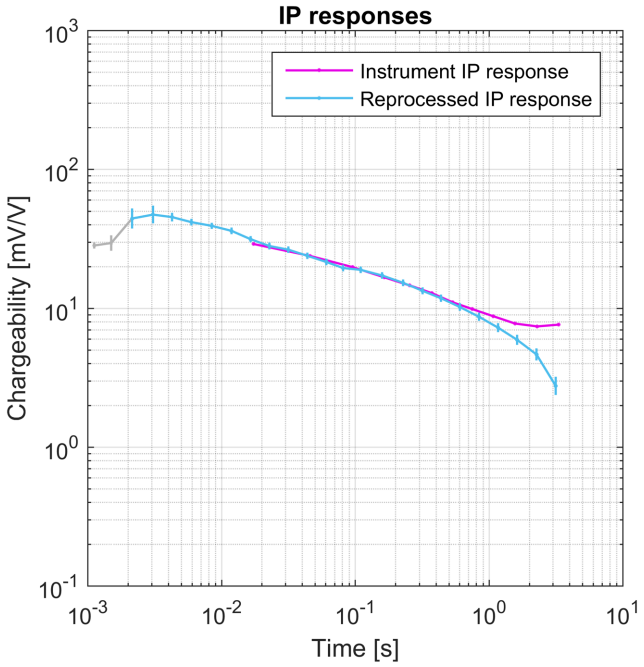


**Figure 9.** IP responses from instrument processing (magenta, instrument output) and from the full-processing scheme presented by this paper (light blue) with error bars corresponding to one STD (vertical lines). The first two gates are greyed out because they contain current switch spikes. In total, six new gates are retrieved by the processing at early times (almost one decade in time), thanks to the harmonic de-noising, and five gates are now usable at late times, thanks to the improved drift removal.

## 4 FULL-FIELD PROFILE PROCESSING EXAMPLE

Fig. 10 shows the pseudo-sections for a full data set (364 quadrupoles, multiple gradient protocol) acquired on the same profile from which the previous IP response example (except Fig. 3) was measured. It shows IP gates 3, 9, 18 and 25 from IP responses generated by the full-signal processing routine and corresponding pseudo-sections for the same gates, but only applying the linear background drift removal. For the early gates, which are not a multiple of the time period of the harmonic noise (gates 3 and 9), there is a remarkable improvement with much smoother pseudo-sections from gate 3 (centre gate time 2.2 ms) and higher. This suggests that with some minor visual inspection and manual filtering, IP data can be used already 2.2 ms after the current pulse is turned off (or changes polarity with 100 per cent duty-cycle acquisition), thus moving the first gate approximately one decade closer to the pulse compared to the traditional IP processing. Contrastingly, IP gate number 18, which is a multiple of the time period of the harmonic noise, shows very similar pseudo-sections for the two processing examples. However, the pseudo-sections for the last IP gate (25), which is known to be affected by the applied drift model, again show differences. Here, the improved processing with Cole–Cole model drift estimate shows a smoother variation in the pseudo-section, especially for the left side of the pseudo-section. In total, 23 usable gates are achieved with the processing described by this paper: compared to the instrument IP response, six gates are gained

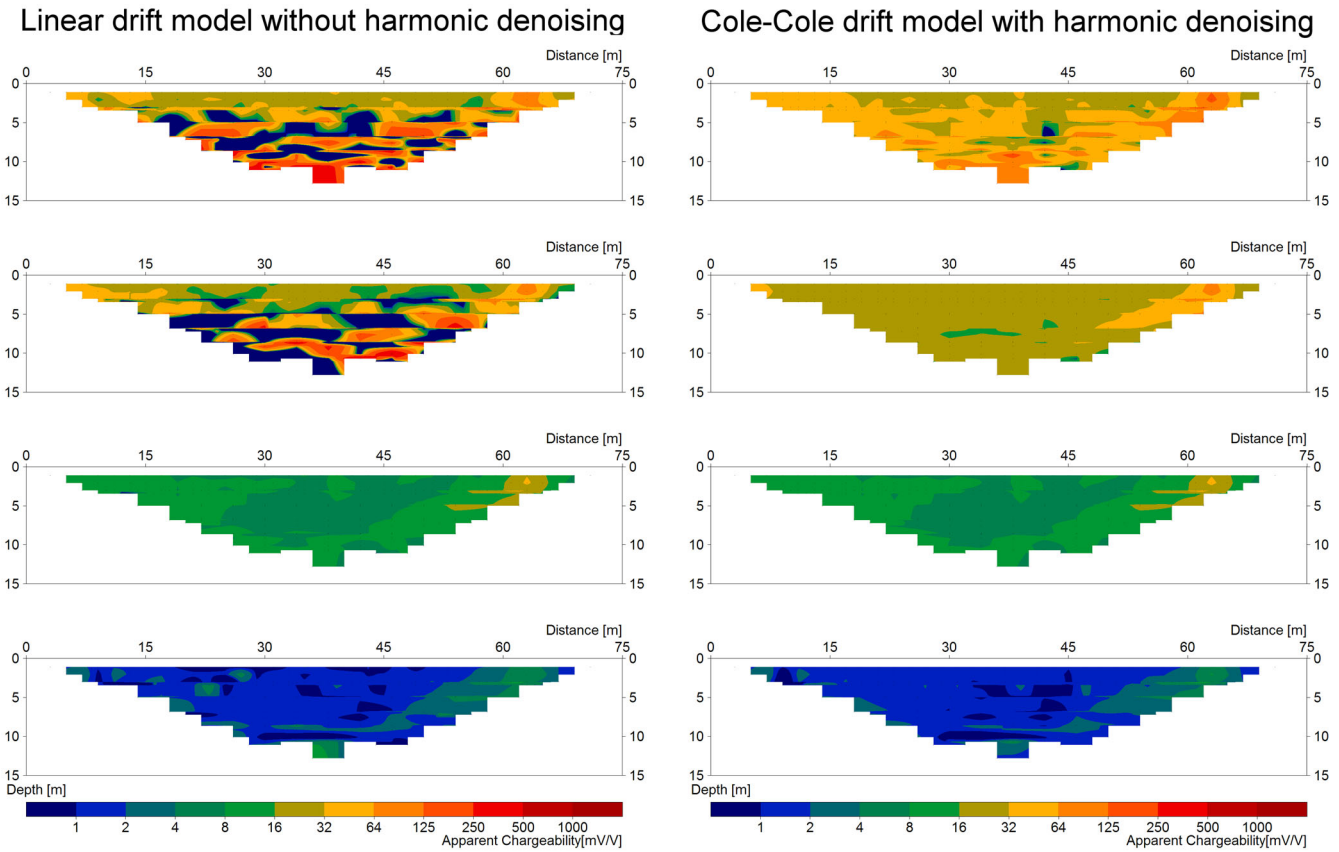


**Figure 10.** Pseudo-sections for IP gates 3, 9, 18 and 25 (from top to down) for processed data without harmonic de-noising and linear drift removal (left) and with harmonic de-noising and Cole–Cole drift removal (right).

at early times and five gates at late times. Altogether, the proposed processing scheme doubles the spectral content of the reprocessed response compared to the instrument processing. The results are just shown for this example profile, but have been confirmed and reproduced on several field surveys carried out in Denmark and Sweden both in urban and rural environments (e.g. Johansson *et al.* 2016).

## 5 CONCLUSIONS

The TDIP signal processing scheme described in this paper significantly improves the handling of background drift, spikes and harmonic noise superimposed on the potential response in the measured full-waveform potential. For cases, where electrodes are used for both transmitting and subsequently receiving, the Cole–Cole background drift removal substantially increases the accuracy of the drift model and recovers the shape of the IP response at late times with significantly reduced bias. In addition, the model-based harmonic de-noising and the data-driven de-spiking give access to early IP response times down to a few milliseconds, which are impossible to retrieve with classic IP processing. Furthermore, the overall SNR is increased by applying tapered and overlapped gates. Finally, data-driven uncertainty estimates of the individual IP gate values are retrieved.

The full-processing scheme presented by this paper has been successfully applied on different datasets from both urban and rural field sites with substantial improvements in spectral information content, data reliability and quality. The increased data reliability and the doubling of the usable range of TDIP data to almost four decades in time will significantly advance the science and the applicability of the spectral TDIP method. In particular, it is a promising development for researchers linking together lab and field measurements, and also for extending the use of the spectral TDIP method as a standard tool outside the research community.

## ACKNOWLEDGEMENTS

Funding for the work was provided by Formas—The Swedish Research Council for Environment, Agricultural Sciences and Spatial Planning (ref. 2012-1931), BeFo—Swedish Rock Engineering Research Foundation (ref. 331) and SBUF—The Development Fund of the Swedish Construction Industry (ref. 12719). The project is part of the Geoinfra-TRUST framework (Transparent Underground Structure). Further support was provided by the research project GEOCON, Advancing GEOlogical, geophysical and CONtaminant monitoring technologies for contaminated site investigation (contract 1305-00004B). The funding for GEOCON is provided by The Danish Council for Strategic Research under the programme commission on sustainable energy and environment. Finally, additional funding was provided by Hakon Hansson foundation (ref. HH2015-0074) and Ernhold Lundström foundation.

## REFERENCES

Abem, 2011. Terrameter LS Product Leaflet [WWW Document]. Available at: http://www.abem.se/support/downloads/technical-specifications/terrameter-ls-leaflet-20111116, last accessed 27 May 2014.

Auken, E. *et al.*, 2015. An overview of a highly versatile forward and stable inverse algorithm for airborne, ground-based and borehole electromagnetic and electric data, *Explor. Geophys.,* **46**(3), 223–235.

Butler, K.E. & Russell, R.D., 1993. Subtraction of powerline harmonics from geophysical records, *Geophysics,* **58**(6), 898–903.

Butler, K.E. & Russell, R.D., 2003. Cancellation of multiple harmonic noise series in geophysical records, *Geophysics,* **68,** 1083–1090.

Chongo, M., Christiansen, A.V., Fiandaca, G., Nyambe, I.A., Larsen, F. & Bauer-Gottwein, P., 2015. Mapping localised freshwater anomalies in the brackish paleo-lake sediments of the Machile–Zambezi Basin with transient electromagnetic sounding, geoelectrical imaging and induced polarisation, *J. appl. Geophys.,* **123**, 81–92.

Cole, K.S. & Cole, R.H., 1941. Dispersion and absorption in dielectrics: I. Alternating current characteristics, *J. Chem. Phys.,* **9**(4), 341–351.

Dahlin, T., 2000. Short note on electrode charge-up effects in DC resistivity data acquisition using multi-electrode arrays, *Geophys. Prospect.,* **48,** 181–187.

Dahlin, T., Leroux, V. & Nissen, J., 2002. Measuring techniques in induced polarisation imaging, *J. appl. Geophys.,* **50,** 279–298.

Dalgaard, E., Auken, E. & Larsen, J.J., 2012. Adaptive noise cancelling of multichannel magnetic resonance sounding signals, *Geophys. J. Int.,* **191,** 88–100.

Davies, L. & Gather, U., 1993. The Identification of Multiple Outliers, *J. Am. Stat. Assoc.,* **88,** 782–792.

Deo, R.N. & Cull, J.P., 2015. Denoising time-domain induced polarisation data using wavelet techniques, *Explor. Geophys.,* **47**(2), 108–114.

Dey, A. & Morrison, H.F., 1973. Electromagnetic coupling in frequency and time-domain induced-polarization surveys over a multilayered earth, *Geophysics,* **38,** 380–405.

Doetsch, J., Fiandaca, G., Auken, E., Christiansen, A.V. & Cahill, A.G., 2015a. Field-scale time-domain spectral induced polarization monitoring of geochemical changes induced by injected $CO_2$ in a shallow aquifer, *Geophysics,* **80**(2), WA113–WA126.

Doetsch, J., Ingeman-Nielsen, T., Christiansen, A.V., Fiandaca, G., Auken, E. & Elberling, B., 2015b. Direct current (DC) resistivity and induced polarization (IP) monitoring of active layer dynamics at high temporal resolution, *Cold Reg. Sci. Technol.,* **119,** 16–28.

Fiandaca, G., Auken, E., Christiansen, A.V. & Gazoty, A., 2012. Time-domain-induced polarization: full-decay forward modeling and 1D laterally constrained inversion of Cole-Cole parameters, *Geophysics,* **77,** E213–E225.

Fiandaca, G., Doetsch, J., Vignoli, G. & Auken, E., 2015. Generalized focusing of time-lapse changes with applications to direct current and time-domain induced polarization inversions, *Geophys. J. Int.,* **203,** 1101–1112.

Fiandaca, G., Ramm, J., Binley, A., Gazoty, A., Christiansen, A.V. & Auken, E., 2013. Resolving spectral information from time domain induced polarization data through 2-D inversion, *Geophys. J. Int.,* **192,** 631–646.

Forsythe, G.E., Malcolm, M.A. & Moler, C.B., 1977. *Computer Methods for Mathematical Computations,* Prentice-Hall.

Gazoty, A., Fiandaca, G., Pedersen, J., Auken, E., Christiansen, A.V. & Pedersen, J.K., 2012a. Application of time domain induced polarization to the mapping of lithotypes in a landfill site, *Hydrol. Earth Syst. Sci.,* **16,** 1793–1804.

Gazoty, A., Fiandaca, G., Pedersen, J., Auken, E. & Christiansen, A.V., 2012b. Mapping of landfills using time-domain spectral induced polarization data: the Eskelund case study, *Near Surf. Geophys.,* **10,** 575–586.

Gazoty, A., Fiandaca, G., Pedersen, J., Auken, E. & Christiansen, A.V., 2013. Data repeatability and acquisition techniques for time-domain spectral induced polarization, *Near Surf. Geophys.,* **11**(4), 391–406.

Harris, F.J., 1978. On the use of windows for harmonic analysis with the discrete Fourier transform, *Proc. IEEE,* **66,** 51–83.

Hönig, M. & Tezkan, B., 2007. 1D and 2D Cole-Cole-inversion of time-domain induced-polarization data, *Geophys. Prospect.,* **55,** 117–133.

Johnson, I.M., 1984. Spectral induced polarization parameters as determined through time-domain measurements, *Geophysics,* **49,** 1993–2003.

Johansson, S., Fiandaca, G. & Dahlin, T., 2015. Influence of non-aqueous phase liquid configuration on induced polarization parameters: conceptual models applied to a time-domain field case study, *J. appl. Geophys.,* **123,** 295–309.

Johansson, S., Sparrenbom, C., Fiandaca, G., Lindskog, A., Olsson, P.-I., Dahlin, T. & Rosqvist, H., 2016. Investigations of a Cretaceous limestone with spectral induced polarization and scanning electron microscopy, *Geophys. J. Int.,* submitted.

Kaiser, J.F., 1990. On a simple algorithm to calculate the "energy" of a signal, in *International Conference on Acoustics, Speech, and Signal Processing,* pp. 381–384, IEEE.

Larsen, J.J., Dalgaard, E. & Auken, E., 2013. Noise cancelling of MRS signals combining model-based removal of powerline harmonics and multichannel Wiener filtering, *Geophys. J. Int.,* **196,** 828–836.

Li, Z.W., Samuelsson, O. & Garcia-Valle, R., 2011. Frequency deviations and generation scheduling in the nordic system, in *2011 IEEE Trondheim PowerTech.,* pp. 1–6, doi:10.1109/PTC.2011.6019176.

Macnae, J.C., Lamontagne, Y. & West, G.F., 1984. Noise processing techniques for time-domain EM systems, *Geophysics,* **49,** 934–948.

Mccracken, K.G., Oristaglio, M.L. & Hohmann, G.W., 1986. Minimization of noise in electromagnetic exploration systems, *Geophysics,* **51,** 819–832.

Mukhopadhyay, S. & Ray, G.C., 1998. A new interpretation of nonlinear energy operator and its efficacy in spike detection, *IEEE Trans. Bio-Med. Eng.,* **45,** 180–187.

Oldenburg, D.W., 1997. Computation of Cole-Cole parameters from IP data, *Geophysics,* **62,** 436–448.

Olsson, P.-I., Dahlin, T., Fiandaca, G. & Auken, E., 2015. Measuring time-domain spectral induced polarization in the on-time: decreasing acquisition time and increasing signal-to-noise ratio, *J. appl. Geophys.,* **123,** 316–321.

Pearson, R.K., 2002. Outliers in process modeling and identification, *IEEE Trans. Contr. Syst. Technol.,* **10,** 55–63.

Pelton, W.H., Ward, S.H., Hallof, P.G., Sill, W.R. & Nelson, P.H., 1978. Mineral discrimination and removal of inductive coupling with multifrequency IP, *Geophysics,* **43,** 588–609.

Peter-Borie, M., Sirieix, C., Naudet, V. & Riss, J., 2011. Electrical resistivity monitoring with buried electrodes and cables: noise estimation with repeatability tests, *Near Surf. Geophys.,* **9,** 369–380.

Revil, A., Binley, A., Mejus, L. & Kessouri, P., 2015. Predicting permeability from the characteristic relaxation time and intrinsic formation factor of complex conductivity spectra, *Water Resour. Res.,* **51,** 6672–6700.

Routh, P.S. & Oldenburg, D.W., 2001. Electromagnetic coupling in frequency-domain induced polarization data: a method for removal, *Geophys. J. Int.,* **145,** 59–76.

Saucier, A., Marchant, M. & Chouteau, M., 2006. A fast and accurate frequency estimation method for canceling harmonic noise in geophysical records, *Geophysics,* **71,** V7–V18.

Welch, P., 1967. The use of fast Fourier transform for the estimation of power spectra: a method based on time averaging over short, modified periodograms, *IEEE Trans. Audio Electroacoust.,* **15,** 70–73.

Zonge, K.L., Wynn, J. & Urquhart, S., 2005. Resistivity, induced polarization, and complex resistivity, *Near Surf. Geophys.,* **9,** 265–300.